

PAPER

A multi-body dynamics based numerical modelling tool for solving aquatic biomimetic problems

To cite this article: Ruoxin Li *et al* 2018 *Bioinspir. Biomim.* **13** 056001

View the [article online](#) for updates and enhancements.

You may also like

- [A multibody approach for 6-DOF flight dynamics and stability analysis of the hawkmoth *Manduca sexta*](#)
Joong-Kwan Kim and Jae-Hung Han
- [The oxymoron of damage assessment in dynamics by static approach](#)
F. Cianetti, M. Palmieri, G. Zucca et al.
- [Multibody Dynamics and Terramechanics-based modeling and simulation of Quarter-Car with Suspension](#)
E Chaturvedi, J Mukherjee and C Sandu

Bioinspiration & Biomimetics



PAPER

A multi-body dynamics based numerical modelling tool for solving aquatic biomimetic problems

RECEIVED
24 January 2018

REVISED
21 May 2018

ACCEPTED FOR PUBLICATION
19 June 2018

PUBLISHED
3 July 2018

Ruoxin Li¹, Qing Xiao¹, Yuanchuan Liu¹, Jianxin Hu², Lijun Li³, Gen Li⁴, Hao Liu^{3,4}, Kainan Hu⁵ and Li Wen⁵

¹ Department of Naval Architecture, Ocean and Marine Engineering, University of Strathclyde, Glasgow, United Kingdom

² Faculty of Mechanical Engineering and Automation, Zhejiang Sci-Tech University, Hangzhou, People's Republic of China

³ Shanghai Jiao Tong University and Chiba University International Cooperative Research Centre (SJTU-CU ICRC), Shanghai Jiao Tong University, Shanghai, People's Republic of China

⁴ Graduate School of Engineering, Chiba University, Chiba, Japan

⁵ School of Mechanical Engineering and Automation, Beihang University, Beijing, People's Republic of China

E-mail: qing.xiao@strath.ac.uk

Keywords: multibody system, self-propulsion, unsteady locomotion, computational fluid dynamics, biomimetics

Abstract

In this paper, a versatile multi-body dynamic algorithm is developed to integrate an incompressible fluid flow with a bio-inspired multibody dynamic system. Of particular interest to the biomimetic application, the algorithm is developed via four properly selected benchmark verifications. The present tool has shown its powerful capability for solving a variety of biomechanics fish swimming problems, including self-propelled multiple degrees of freedom with a rigid undulatory body, multiple deformable fins and an integrated system with both undulatory fish body and flexible fins. The established tool has paved the way for future investigation on more complex bio-inspired robots and live fish, for either propulsion or manoeuvring purposes.

1. Introduction

Fish have evolved excellent propulsive and manoeuvring abilities that have allowed them to adapt to the aquatic environment and survive the natural selection process. For humans, the physical and biological mechanisms observed in swimming fish are a precious source of inspiration for the development of artificial swimming machines such as autonomous underwater vehicles [1, 2].

Generally, there are two effective ways to study fish swimming mechanisms, namely through experimental study and simulation. These methods are well summarised in several comprehensive review papers [3–7]. The experimental approach observes and measures the locomotion of live or robotic fish, and provides the most reliable data for analysis and direct evaluation of the robots [8–13]. Benefitting from newly developed measuring techniques, the experimental approach can directly record fluid motion via PIV measurement [14, 15]. However, some other key physical parameters which are beyond the capability of experimental records remain unresolved (such as the surface stress of a swimming fish). While an experimental approach can deal with the morphological, behavioural and

environmental complexities in nature, these complexities sometimes hinder researchers' ability to arrive at mathematical principles.

To compensate for these experimental tests, computational approaches have been adopted. The approaches can be divided into analytical models and computational fluid dynamics (CFD) models. The analytical model reduces the complexity of live fish swimming during the modelling process, considering that a swimming fish is in quasi-steady state. As such, this method concentrates on the primary fluid dynamic characteristics while neglecting secondary effects (e.g. Lighthill's Elongated Body Theory simplifies the fish body as a curve and assumes a completely inertial flow condition [16]). This results in elegant mathematical expressions which can be solved without computers. Therefore, such simplifying assumptions in the analytical model enable us to expediently analyse the essence of swimming, albeit at a considerable sacrifice of applicable range and accuracy. Particularly, as the unsteady mechanism is found to cause considerable extra hydrodynamic force, this is beyond the capability of any analytical model (e.g. [17]).

Up-to-date CFD models can complement the role of experimental and analytical models but are

also capable of executing independent missions. In all research and engineering areas concerning fluid dynamics, CFD model predictions have been validated against experimental observations to demonstrate their accuracy.

Distinct from a traditional CFD arrangement via fixing a swimming object in an incoming flow condition (equivalent to a water-tunnel experiment, commonly used in some commercial CFD software), present fish CFD simulations tend to allow the fish propelling themselves through water (free-swimming) [18–20]. While the self-propelling (free-swimming) arrangement requires additional coupling of hydrodynamics and body-dynamics, this method has several significant advantages. For example, the swimming speed is no longer treated as a known input beforehand, and thus the predicted CFD results are able to explore the kinematic and morphological parameter map beyond experimental observation (e.g. [17]). In addition, the CFD studies do not need to be limited to any stable forward motion, instead it can be expanded to various unstable or manoeuvre situations (e.g. [21, 22]).

Apart from the above-mentioned advantages, the complexity of the CFD objectives in this study have been significantly improved. Traditionally, with the increase of complexity, the studies on fish swimming can be classified into three major groups: (a) fish body undulation without considering the influence of fins; (b) single fin, such as caudal fin or multiple fins ignoring the fish body; and (c) a combined fish body with multiple fins. A brief review of the studies in the relevant areas are given in the following section.

For the first category, typical modes such as anguilliform and carangiform are introduced [5]. The anguilliform swimmer, such as the eel, bends its body into a wave shape, with the wave propagating from the fish head to the tail. To analyse this problem, a fish body can be modelled either through a continuous body or a multi-body system with several discrete elements connected via joints. Typical examples include the work from Kern and Koumoutsakos [18], Carling *et al* [19] and Eldredge [23]. The carangiform mode fish, unlike the anguilliform mode, undulates the last third portion of their body along with a caudal fin. The relevant studies can be found from the papers of Maertens *et al* [24], Ogata *et al* [25] and Curatolo and Teresi [26].

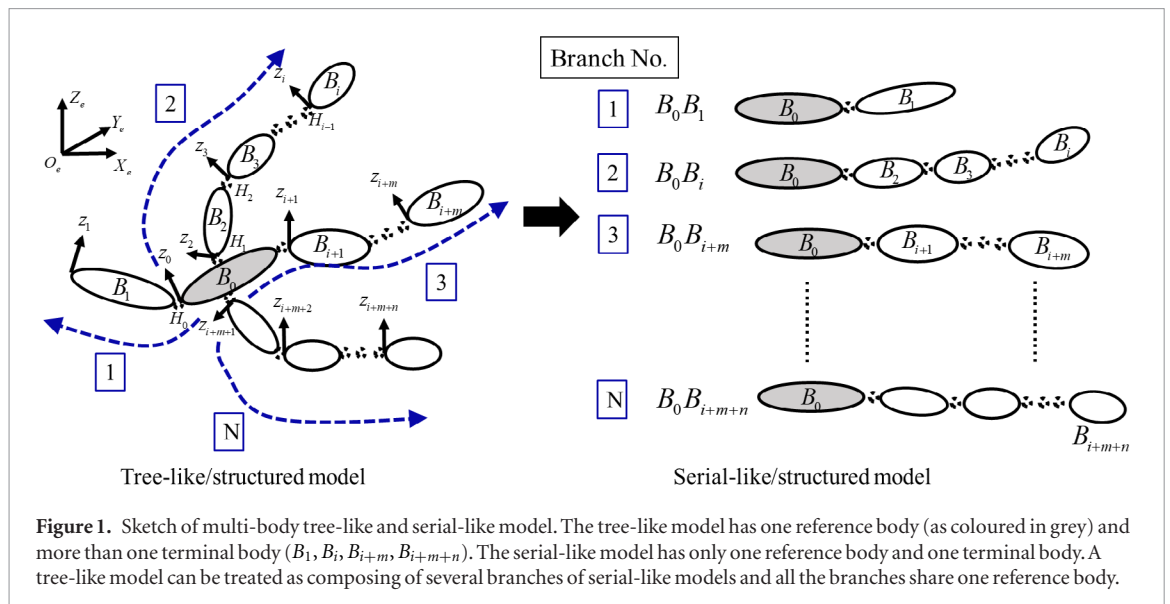
In contrast to the first category focusing on a fish body, some numerical investigations concentrated on the performance of a single fish fin or of a fin–fin interaction (single fin: [27, 28]; passively deformable fin: [29]; rayed fin: [30, 31]; and fin–fin interaction: [32, 33]).

Apart from the above two groups, other researchers investigated a combined model for a fish with lateral (paired fins such as pectoral fins) or median fins (unpaired fins such as dorsal, anal and caudal fins). Borazjani [34] examined the function of median fins during C-start by reconstructing the model with/

without fins using an Immersed Boundary Method. Their results concluded that the anal and dorsal fins played a more significant role in the stability of the fish during C-start mode than in producing hydrodynamic propulsion force. However, although the fins moved with the body of fish, their individual undulation was not considered in this study. Similarly, using an IBM method, Han *et al* [35] investigated the dorsal and anal fins of a sunfish model during a cruising condition. It was found that with dorsal, anal and caudal fins, the fish has a greater efficiency compared to other conditions with only two fins. The deformation of fins was imposed by prescribing the kinematic motion, and a constant incoming velocity was given rather than as a result of fluid-structure interaction modelling. Xu and Wan [36] numerically simulated a self-propelled fish swimming with a pair of rigid pectoral fins using a multi-block and overset grid method. The rowing, feathering and flapping motions of the fins were investigated. Numerical results showed that during the turning motion, both hydrodynamic moment and lateral force were generated by the fins. The deformation of the pectoral fins was not included in this work.

It is noted from the above studies that numerical simulations on biomimetic self-propelled fish with multiple deformable fins are still in their infancy and thus require further development. In this study, we aim to develop a mature and effective numerical modelling tool which can simulate a self-propelled fish combining its multiple rigid/deformable fins. To achieve a comprehensive analysis, a multi-body dynamics (MBD) theory-based algorithm is introduced. According to the definition given by Khalil and Dombre [37], a general model in the present algorithm can be referred to as a tree-like/structured model in contrast to a serial-like/structured model. For both tree- and serial-like models, they are composed of n elements and $n - 1$ hinges as given in figure 1. A reference body B_0 is selected and used as a starting element for both models. The primary difference between the two models is that, in a serial-like model, the n th element is the terminal body, whereas, a tree-like model has more than one terminal body. As demonstrated in figure 1, several branches exist in a tree-like model and each branch can be treated as a serial-like model.

The present study succeeds and improves on the research of Hu [38, 39], whereby a serial-like MBD solver, based on a hybrid mobile multi-body algorithm [40–42] is combined with a CFD tool to investigate a simplified 2D self-propelled fish. Hu's method can mimic a swimming body as a series of discrete elements in a sequence with a motion actuating mechanism that can be either passive or active. However, because of the nature of a series arrangement, the fish fin is unable to be included. In addition, Hu's model can only deal with a rigid element, which restricts each element in the system to follow a uniform undulating locomotion. In the present study, the algorithm is further developed and upgraded to handle tree-like



structures, such as a fish body with multiple fins. Thus, it can be widely applied to various fish swimming problems, such as the undulating locomotion of a fish body with single and multiple fins. In addition, the elements in the updated MBD model can be regarded as either rigid or deformable, which makes the numerical modelling of deformable fins possible.

To describe this new model and validate its capability, the remainder of the paper is structured as follows. Section 2 will introduce in detail the tree-like MBD algorithm, the fluid solver and the coupling between the two. Section 3 will present four canonical examples to illustrate the application of our developed numerical tool, including the comparison with some available experimental and CFD results. This will cover a discrete eel-like model, a continuous eel-like body, a peduncle-caudal-fin and a self-propelled fish swimming induced by its multiple fin undulation.

2. Numerical methods

In this section, detailed description on the established numerical methodology will be introduced. The fluid flow around fish and fins is solved using Commercial software ANSYS Fluent 15.0. To cope with the complex body and multiple rigid and/or deformable fins locomotion, as explained fully in section 2.1, dynamics of the model are solved using multi-body tree-like algorithms. This part is developed with an in-house code and embedded into user defined function (UDF) of ANSYS Fluent. At each time step, data exchange occurs between the fluid solver and the in-house code.

2.1. Multi-body dynamics algorithm

The biomimetic problem to be solved is complicated and can include multiple degrees of freedom related locomotion of a fish body, such as translation and rotation. Fish forward motion induced by the undulation of the body or fins is also one of the numerical FSI solutions. In addition, fish fins may

undergo independent locomotion, which is different from the main body. It is thus very challenging to use traditional rigid body dynamics to solve this problem. To cope with this, the dynamics of the model is handled by a MBD method based on previous work [9, 39, 40]. Primarily, at each time step, the fluid force applied on each element/body in the MBD model is obtained from the fluid solver and passed to our in-house code. The overall force on the entire model is the accumulation of all relevant elements. With the use of Newton's Second Law, the entire dynamic model acceleration is determined. By integrating once and twice with time, the velocity and location relative to the global coordinate is obtained, respectively. The above process always starts with a specified reference body (see figure 1), then to each element along different branches based on a Euler transformation matrix and hinge constraints which will be described in the following sections.

2.1.1. Model description

The whole model is considered as being constructed with several separate elements/bodies as given in figure 1. These elements can be either rigid or deformable. In the present algorithm, the deformation of elements is achieved by prescribing the motion at each grid point on the surface of elements. There are two types of coordinate in this system, i.e. global coordinate O_e and local coordinates O_i . The reference body B_0 is specified and coloured in grey. Several branches exist, indicated by blue arrow dashed lines, relative to the reference body B_0 . Apart from the reference body B_0 , other elements in the branches are given numbers in the orders of 1 to the last element. Two adjacent elements are connected with one virtual hinge H_i . At each hinge, there is only one degree of freedom motion that can be imposed, i.e. rotational motion about local z axis. By adding more than one virtual hinge, multi-degrees of freedoms can be achieved. For the model consisting of rigid elements,

prescribed rotational acceleration $\ddot{\theta}_i$ can be provided at each hinge so that within one time step the angular velocity $\dot{\theta}_i$ and angle θ_i at each hinge is known. In terms of a system with deformable elements, the hinge motion is zero, i.e. there is no relative rotational motion between two adjacent elements connected by the hinge. An index vector a is employed to store element/body connection information, which is vital for a tree-like MBD system.

2.1.2. Euler transformation

Transformation between two successive local coordinates is completed based on the Newton–Euler Frame. A homogeneous transformation matrix jT_i which transforms the initial location/position from a local coordinate of body $B_i(O_i, x_i, y_i, z_i)$ to $B_j(O_j, x_j, y_j, z_j)$ is defined as:

$${}^jT_i = \text{rot}(x_i, \alpha_j) \text{trans}(x', d_j) \text{rot}(z'', q_j) \text{trans}(z^*, r_j) = \begin{pmatrix} \cos q_j & -\sin q_j & 0 & d_j \\ \cos \alpha_j \sin q_j & \cos \alpha_j \cos q_j & -\sin \alpha_j & -r_j \sin \alpha_j \\ \sin \alpha_j \sin q_j & \sin \alpha_j \cos q_j & \cos \alpha_j & -r_j \cos \alpha_j \\ 0 & 0 & 0 & 1 \end{pmatrix}. \tag{1}$$

Referring to figure 2, transformations operate along the x and z axis in order. The local coordinate of body $B_i(O_i, x_i, y_i, z_i)$ firstly rotates around the x_i axis with an angle of α_j , translates along the x' axis with a distance of d_j , then rotates about the z'' axis with an angle of q_j , and translates along z^* axis with the distance r_j to get the final local coordinate of body $B_j(O_j, x_j, y_j, z_j)$.

When the angular motions θ_a on the hinge connecting two consecutive bodies is specified, the transformation matrix ${}^jT_i(\theta_a)$ is divided into one (3×3) rotation matrix ${}^jR_i(\theta_a)$ and one (3×1) position vector jP_i as:

$${}^jT_i(\theta_a) = \text{rot}(x_i, \alpha_j) \text{trans}(x', d_j) \text{rot}(z'', q_j + \theta_a) \text{trans}(z^*, r_j) = \begin{pmatrix} {}^jR_i(\theta_a) & {}^jP_i \\ 0 & 1 \end{pmatrix}. \tag{2}$$

The angle θ_a is determined by looking through the index vector a . An adjoint map operator Ad_{jg_i} is introduced for the transformation of inertia, force and velocity from body B_i to body B_j and is defined as:

$$Ad_{jg_i} = \begin{pmatrix} {}^jR_i(\theta_a) & {}^jR_i(\theta_a) {}^i\hat{P}_j^T \\ 0 & {}^jR_i(\theta_a) \end{pmatrix}. \tag{3}$$

${}^i\hat{P}_j$ is a (3×3) skew-symmetric tensor and can be obtained from the (3×1) position vector iP_j .

2.1.3. Force and acceleration

The fluid force of each element is obtained by fluid solver at each time step and notated as a (6×1) force vector $F_{ext,j}$, including force and moment in three directions. The net force β_j^* on the terminal body is defined as:

$$\beta_j^* = \beta_j - F_{ext,j} \tag{4}$$

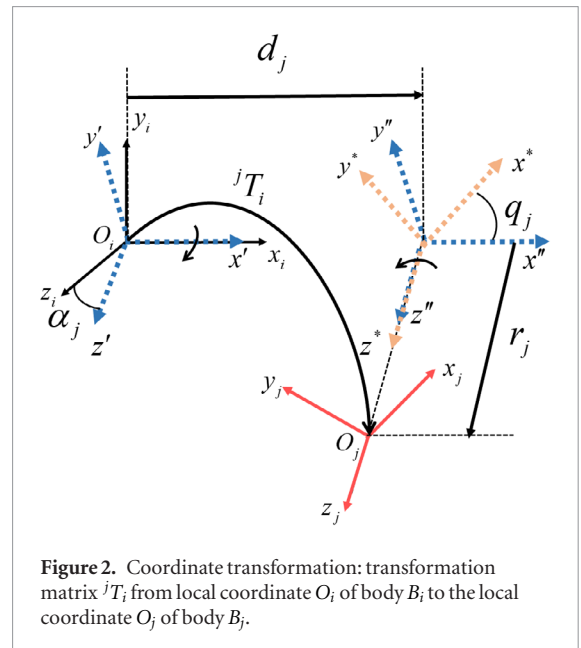


Figure 2. Coordinate transformation: transformation matrix jT_i from local coordinate O_i of body B_i to the local coordinate O_j of body B_j .

where β_j is a (6×1) Coriolis and centrifugal forces vector. For detailed derivation, refer to Porez et al [9]. The inertia tensor M_j consists of a (3×3) tensor of body mass M_j , two (3×3) tensors of first inertia moments $M\hat{S}_j$ and a tensor of angular inertia I_j :

$$M_j = \begin{pmatrix} M_j & -M\hat{S}_j \\ M\hat{S}_j & I_j \end{pmatrix}. \tag{5}$$

As body B_i is followed by body B_j , the inertia tensor and force between these two bodies is linked by the following equations:

$$M_i^* = M_i + Ad_{jg_i}^T M_j^* Ad_{jg_i} \\ \beta_i^* = (\beta_i - F_{ext,i}) + Ad_{jg_i}^T (M_j^* (A\ddot{\theta}_j + \zeta_j) + \beta_j^*). \tag{6}$$

Here, A is a (6×1) unit vector, $\ddot{\theta}_j$ is the angular acceleration on hinge j , ζ_j represents the acceleration induced by the acceleration transformation between local coordinates of two successive bodies [40].

By accumulating the force and inertia tensor from the terminal body back to the reference body, the acceleration η_0 of reference body B_0 in the local coordinate can be estimated as:

$$\eta_0 = -(M_0^*)^{-1} \beta_0^*. \tag{7}$$

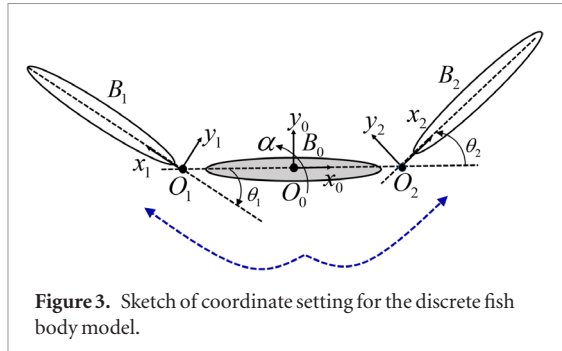
2.1.4. Velocity and position

The status of the whole system relative to the earth coordinate is decided by the reference body $B_0(O_0, x_0, y_0, z_0)$. Its velocity η_0 in the local coordinate is solved using the 4th order Runge–Kutta scheme as follows:

$$\eta_0|_{t+\Delta t} = \begin{pmatrix} V_0|_{t+\Delta t} \\ \Omega_0|_{t+\Delta t} \end{pmatrix} = \eta_0|_t + \frac{\Delta t}{6} \left(\dot{\eta}_0|_t^1 + 2 \dot{\eta}_0|_{t+\frac{\Delta t}{2}}^2 + 2 \dot{\eta}_0|_{t+\frac{\Delta t}{2}}^3 + \dot{\eta}_0|_{t+\Delta t}^4 \right) \tag{8}$$

Table 1. Summary of the case studies.

Case No.	Problem type		Dimension	Rigid/deformable element in model	Algorithm type
1	Fish body undulation	Discrete model	2D	Rigid	Tree-like
2		Continuous model	2D	Rigid	Serial-like
3	Single caudal fin		3D	Rigid + Deformable	Serial-like
4	Fish with multiple fins		3D	Rigid + Deformable	Tree-like

**Figure 3.** Sketch of coordinate setting for the discrete fish body model.

where V_0 and Ω_0 represent a (3×1) linear vector and a (3×1) angular velocity vector in the x, y, z direction. The velocity η_0 of the reference body in the local coordinate can be transferred to the earth coordinate as:

$${}^e\eta_0 = {}^eR_0\eta_0 \quad (9)$$

where eR_0 is a (3×3) matrix associated with the orientation of the reference body. With a (3×1) position vector eP_0 , the transformation matrix eT_0 between the earth coordinate and the reference body is:

$${}^eT_0 = \begin{pmatrix} {}^eR_0 & {}^eP_0 \\ 0 & 1 \end{pmatrix}. \quad (10)$$

Velocity for the other bodies is calculated recursively from the reference body forward to the terminal body. The transformation of velocity η from an anterior body B_i to its following body B_j is defined as:

$$\eta_j = A d_{j_g} \eta_i + \dot{\theta}_j A, \quad (11)$$

where $\dot{\theta}_j$ is the angular velocity of the hinge j connecting bodies B_i and B_j .

The position of other bodies relative to the global coordinate is also obtained by transforming from the reference body forward to the terminal body using the following equation:

$$\begin{aligned} {}^eT_j &= {}^eT_i {}^iT_j(\theta_a) \\ &= \begin{pmatrix} {}^eR_j & {}^eP_j \\ 0 & 1 \end{pmatrix} \end{aligned} \quad (12)$$

where eT_i and eT_j are the transformation matrices for bodies B_i and B_j ; eR_j and eP_j are the orientation matrix and position vector of body B_j . All the variables are in the earth coordinate.

2.2. Fluid solver

As mentioned earlier, the fluid flow around fish and fins are solved using ANSYS Fluent, a finite volume

method (FVM) CFD tool. The governing equations are incompressible continuity and momentum equations:

$$\begin{aligned} \frac{\partial \vec{u}}{\partial t} + (\vec{u} \cdot \nabla) \vec{u} &= -\frac{1}{\rho} \nabla p + \frac{\mu}{\rho} \nabla^2 \vec{u} \\ \nabla \cdot \vec{u} &= 0 \end{aligned} \quad (13)$$

where $\vec{u} = (u, v, w)$ is the fluid velocity vector, p is the fluid pressure, μ is the fluid viscosity and ρ is the fluid density. The present study assumes that flow is laminar.

Pressure–velocity coupling is achieved by enabling non-iterative time advancement (NITA) and the selection of the fractional step method (FSM), as the NITA scheme can reduce the splitting error by using sub-iterations per time step and thus computes quicker than iterative time advancement (ITA) by performing only a single outer iteration per time-step. In FSM, momentum equations are decoupled from the continuity equation. A first-order implicit time marching scheme is adopted for the transient terms. In terms of spatial discretization, a Least Squares Cell Based approach is employed for the gradient. A second-order scheme is used for pressure interpolation to improve accuracy. The second-order upwind scheme is employed for diffusive term discretization.

Due to the large deformation of the mesh when fish swim, the dynamic mesh function available in Fluent is used. As a body in the Multi-Body system could be considered as either rigid or deformable, different forms of User Defined Functions are used for the dynamic mesh zones. Given rigid bodies, the velocity of each body should be imported to Fluent. As for deformable bodies, the position of every mesh node on the deformable body surface is calculated in the MBD code and given to Fluent at each time step. These variables are relative to the global coordinate.

2.3. Coupled algorithm

At each time step, the transfer of data is needed between the fluid solver and UDF. At the beginning of each time step, the velocity and position of each body relative to the global coordinate is transferred to Fluent to calculate the fluid force around the model. Such information is then delivered back to the MBD code to predict the velocity and position of the fish at the next time step.

A vector $\mathfrak{R}(X_{state}, \dot{\theta}_j, \theta_j)$ collects the status X_{state} of reference body B_0 , the angular velocity $\dot{\theta}_j$ and the angle θ_j of all the hinges, j in total, in a model:

$$\mathfrak{R}(X_{state}, \dot{\theta}_j, \theta_j) = \mathfrak{R}({}^eV_0, {}^e\Omega_0, {}^eP_0, {}^eQ_0, \dot{\theta}_j, \theta_j). \quad (14)$$

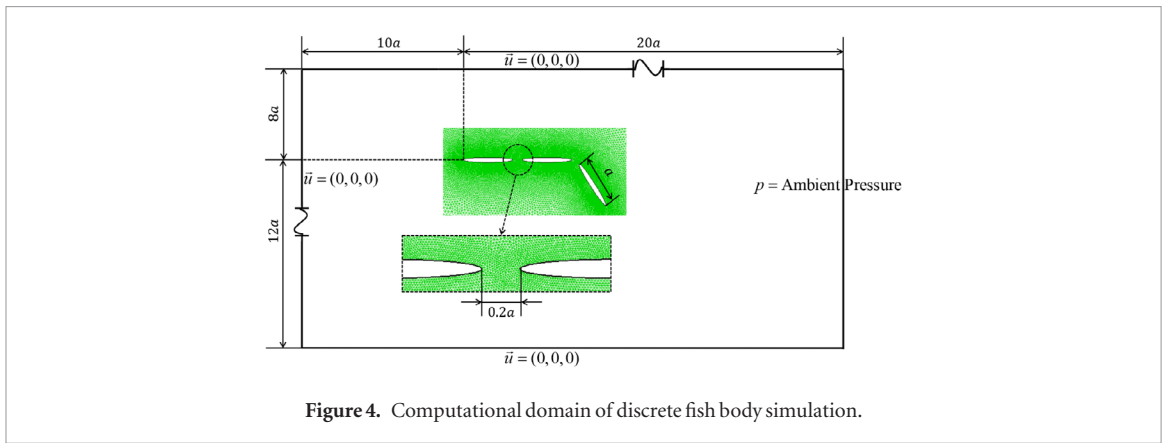


Figure 4. Computational domain of discrete fish body simulation.

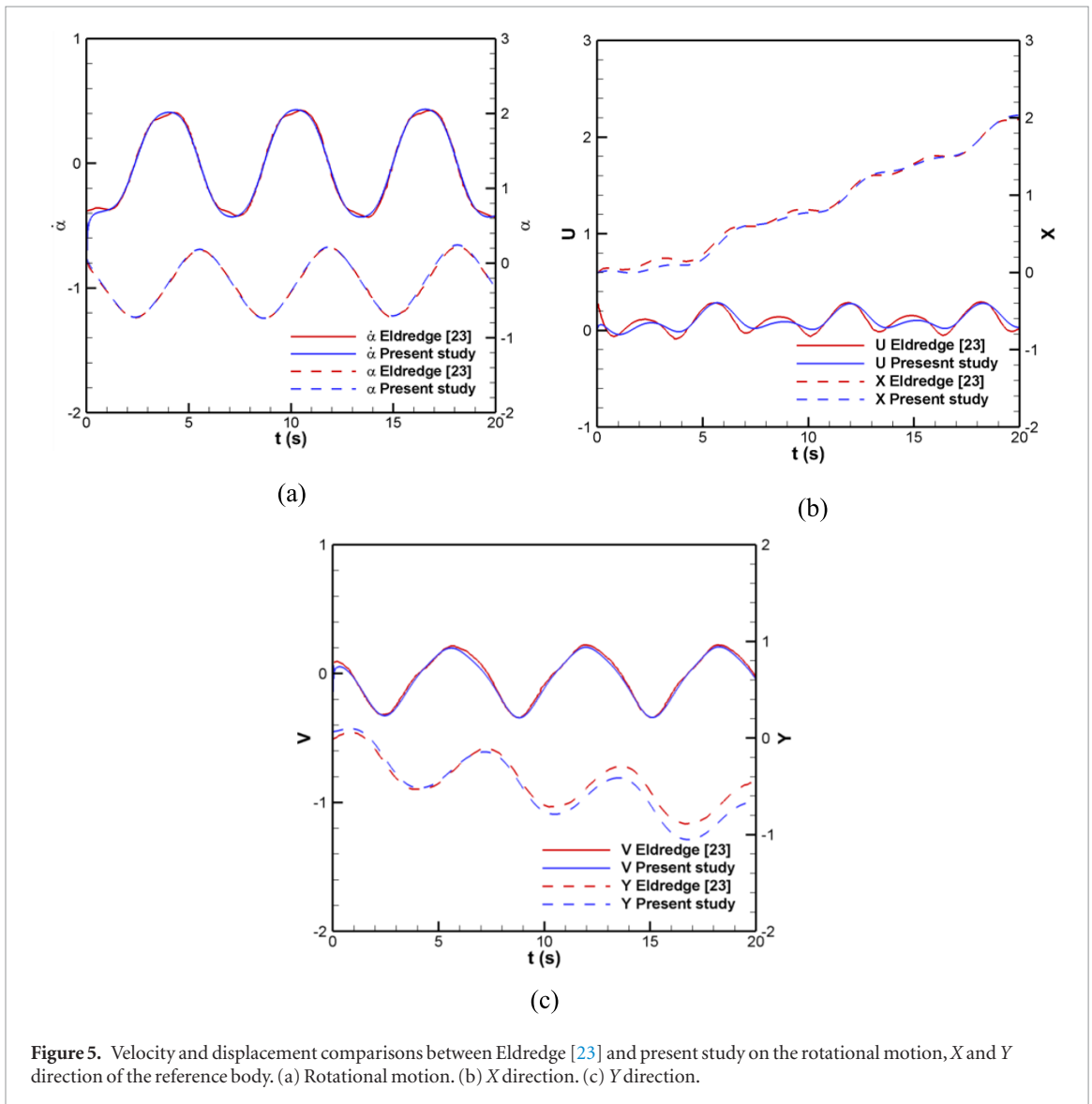


Figure 5. Velocity and displacement comparisons between Eldredge [23] and present study on the rotational motion, X and Y direction of the reference body. (a) Rotational motion. (b) X direction. (c) Y direction.

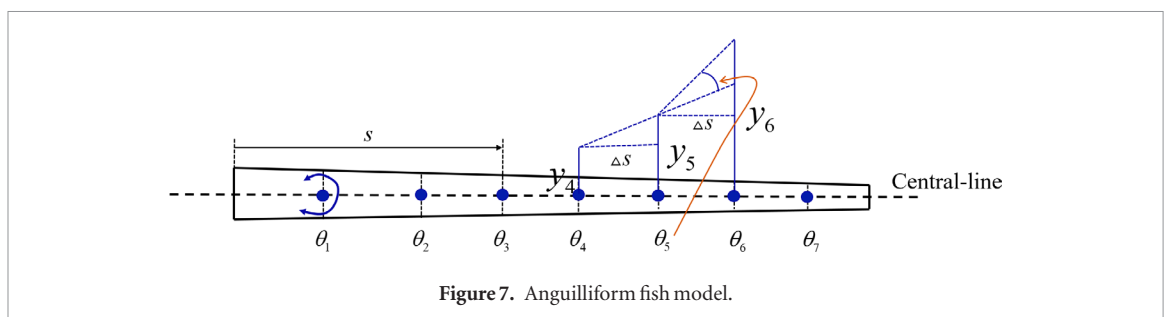
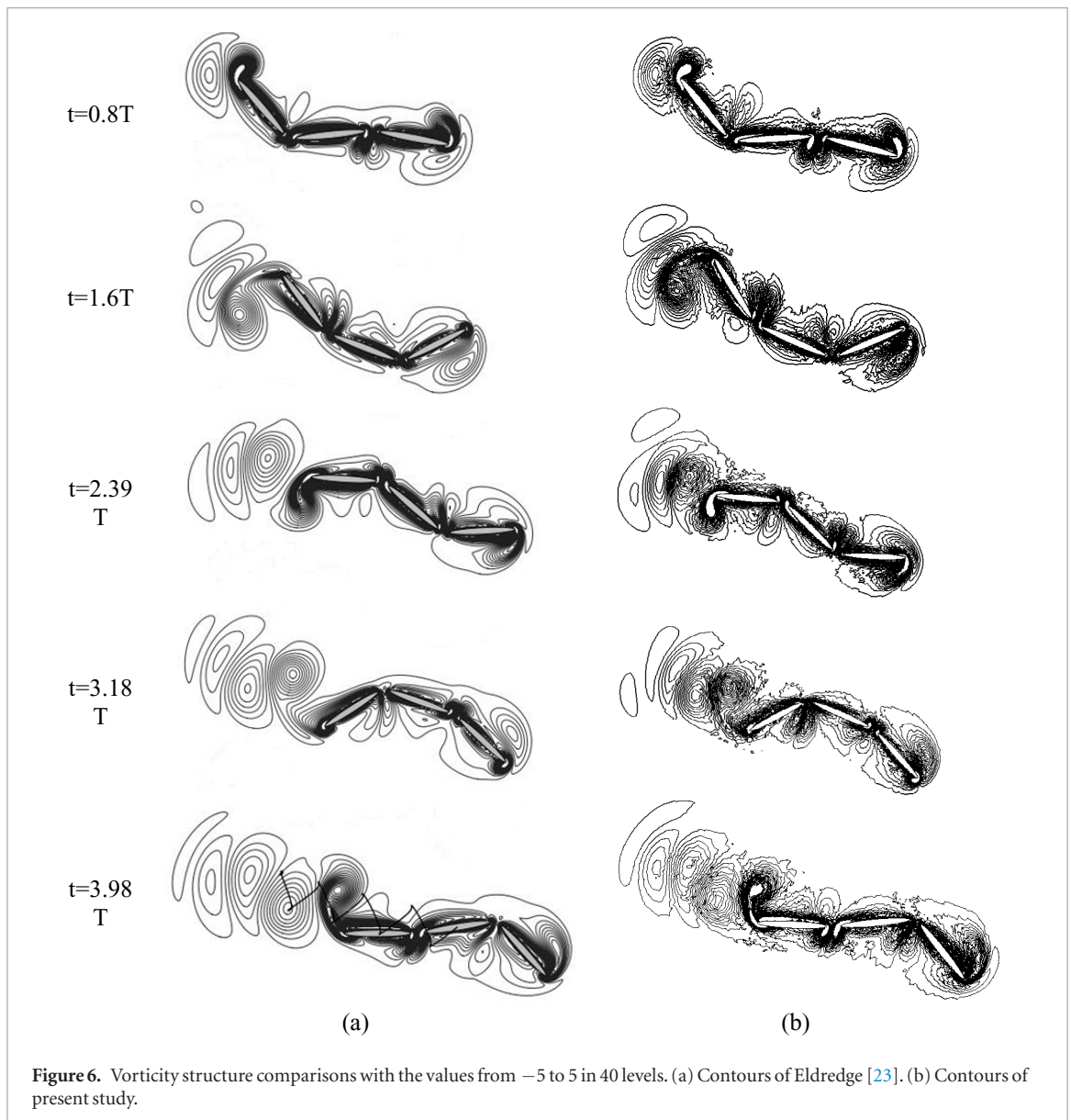
Generally, to predict a new time step, a 4th order Runge–Kutta explicit time discretization is employed as:

$$\mathfrak{R}|_{t+\Delta t} = \mathfrak{R}|_t + \frac{\Delta t}{6} (\dot{\mathfrak{R}}|_t + 2\dot{\mathfrak{R}}|_{t+\Delta t/2}^2 + 2\dot{\mathfrak{R}}|_{t+\Delta t/2}^3 + \dot{\mathfrak{R}}|_{t+\Delta t}^4). \quad (15)$$

Here, Δt stands for time step size.

3. Case studies

Four problems are used to validate the numerical methodology described in section 2, as summarised in table 1. In particular, (a) an undulating self-propelled discrete eel-like swimming model; (b) a self-propelled continuous eel-like swimmer; (c) a fish robot with caudal fin cupping motion; (d) a self-propelled fish driven by its multiple deformable fins. These problems



cover FSI induced forward motion, combined fish body and fins as well as rigid and deformable fins.

3.1. Discrete fish body undulation

By modelling a fish as several articulated solid bodies, Kano *et al* [47] first analysed its locomotion in ideal fluid. Furthermore, Eldredge [23] simulated a simplified undulation motion of an anguilliform free-swimming fish with a two-dimensional model made of three identical rigid elements. This can be considered as splitting a continuous eel-like fish

body into several separate elements connected by joints. The geometric shape of each element is ellipse, with an aspect ratio of major versus minor axis of 10. The length of each element is a , and the distance d between each body is $0.2a$. To use our MBD method, the middle body is selected as the reference body B_0 , the other two bodies, numbered as B_1 and B_2 , are treated in two different branches. The local coordinate system for each body is illustrated in figure 3. In order to obtain comparable results with the previous study, the rotational angular motions (θ_1

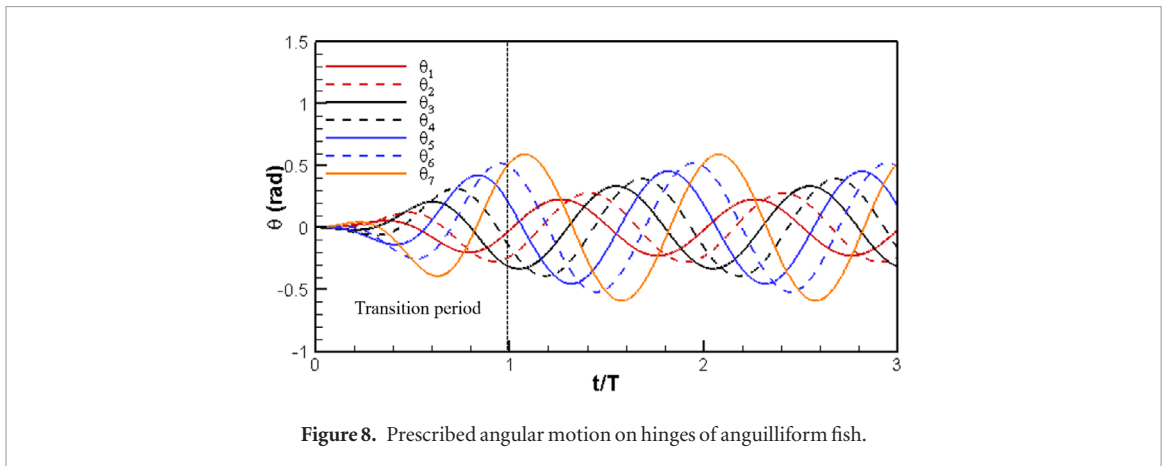


Figure 8. Prescribed angular motion on hinges of anguilliform fish.

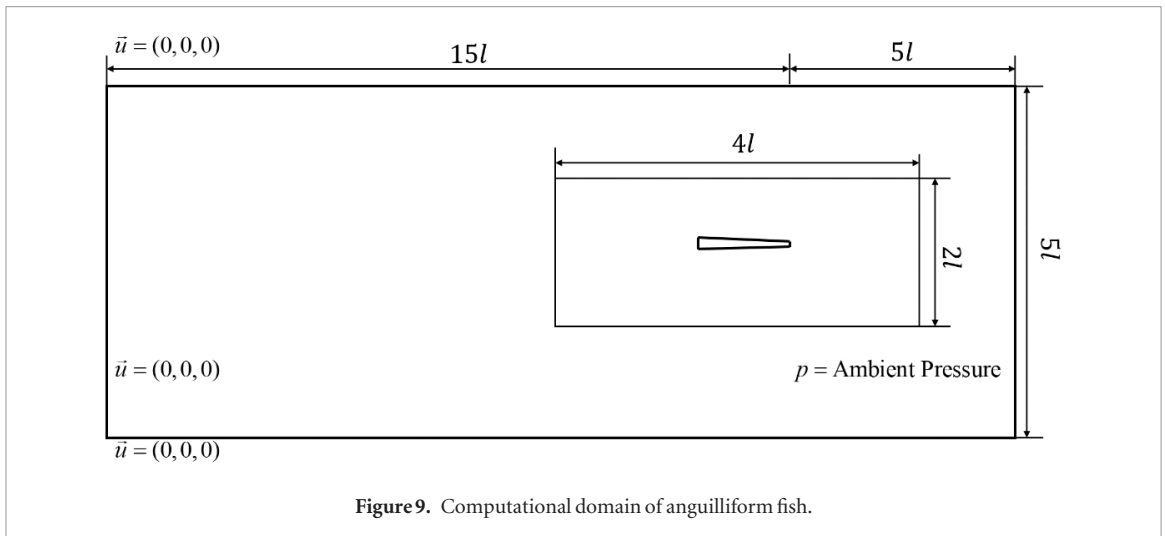


Figure 9. Computational domain of anguilliform fish.

and θ_2) are specified between two adjacent bodies (B_0 and B_1 , B_0 and B_2) as:

$$\begin{aligned} \theta_1(t) &= \cos(t - \frac{\pi}{2}) \\ \theta_2(t) &= -\cos(t). \end{aligned} \quad (16)$$

An undulation Reynolds number [23] is used in the present study and is equal to 200 via the following equation:

$$Re = \frac{\dot{\theta}_{max} a^2}{\nu} \quad (17)$$

where $\dot{\theta}_{max}$ is the maximum angular velocity, a is the length of each ellipse, and ν is the kinematic viscosity.

The computation is performed in a domain with a size of $30a \times 20a$, shown in figure 4, which is large enough to avoid the boundary influence. The model is placed $10a$ and $8a$ away from the inlet and upper boundary, respectively. Around the model, a small inner zone is designed to better capture the vortex structure around the swimming body. Unstructured triangular meshes are applied to the whole computational domain and the overall grid number is around 141 000. At the surface of the three elements, no slip boundary conditions are imposed. A constant velocity ($\vec{u} = (0, 0, 0)$) are set to the left, upper and lower boundary and the pressure at the right boundary is set to ambient pressure. Time step is set as $\Delta t = \frac{T}{500}$ after testing, where T is the undulating period.

Detailed comparison of results between the present study and Eldredge [23] is given in figures 5 and 6. It should be noted that, the whole numerical model is free in X and Y directions, while a rotational motion is possible for the central element. Figure 5 displays the comparison between the present study and in terms of the induced rotational angle α , the angular velocity $\dot{\alpha}$, and the velocity and displacement in X and Y direction at the central point O_0 of body B_0 , normalized either by the body length a or velocity $\dot{\theta}_{max} a$. The induced velocity is periodic for both rotational ($\dot{\alpha}$) and translational (U and V) motion. The mean linear velocity is positive for U and negative for V , and hence the undulating fish moves towards the positive X and negative Y direction. Meanwhile, the displacement in the Y direction is smaller and more oscillated than that in the X direction. For rotational motion, the rotational angle α varies from an approximate -0.8 rad to 0.2 rad.

Figure 6 is the vorticity field comparison at five instantaneous times. The foremost element generates vortex, which moves backwards from two sides and merges with the boundary layer. The vortex sheds off at the tip of body B_1 and obvious vortex street can be observed in the downstream of the model. Overall a good comparison with the previous study is clearly demonstrated.

The successful validation of applying our MBD algorithm to this discrete model is vital in the bio-

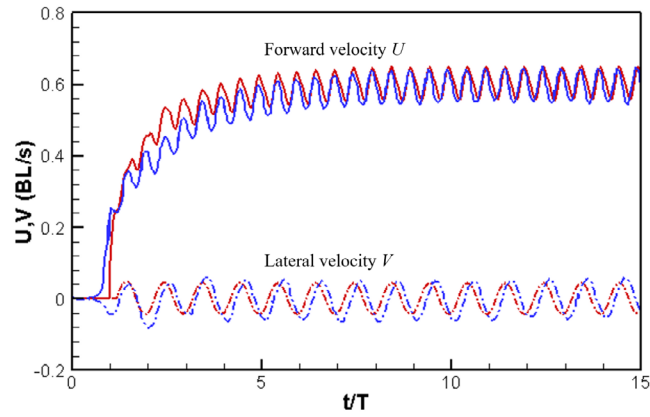


Figure 10. Velocity comparisons (blue lines: results of Carling *et al* [19]; red lines: present results).

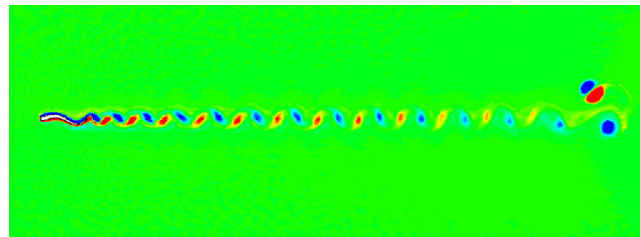


Figure 11. Vorticity contour for 15 undulating periods (z vorticity with the values from -3 to 3 in 20 intervals).

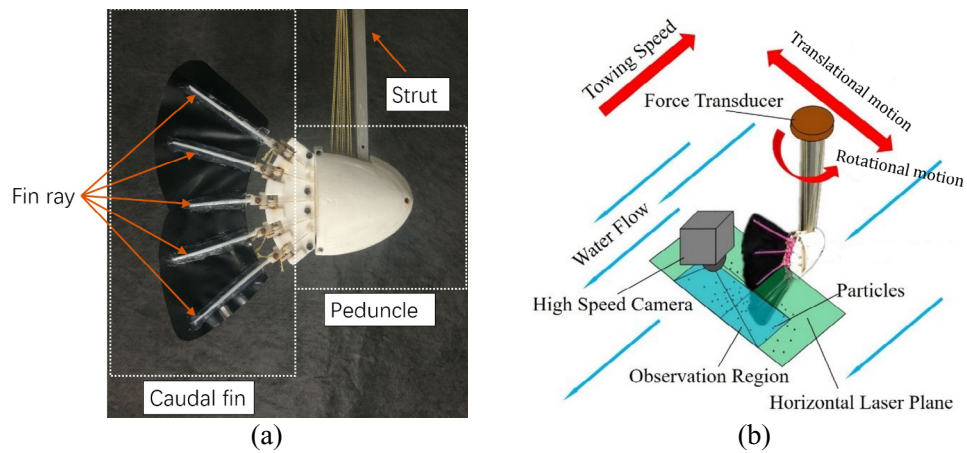


Figure 12. Experimental model of fish peduncle-caudal [43]. (a) Component of model. (b) Sketch of experiment.

inspired robot area, as most anguilliform robot fish are made of a series of modules with motion control actuators placed between two adjacent modules, such as AmphiBot III [9].

3.2. Continuous Anguilliform fish undulation

To demonstrate that the established MBD is also applicable to modelling continuous body locomotion like an anguilliform mode, a 2D self-propelled eel-like fish model is selected in this section, which is taken from Carling *et al* [19].

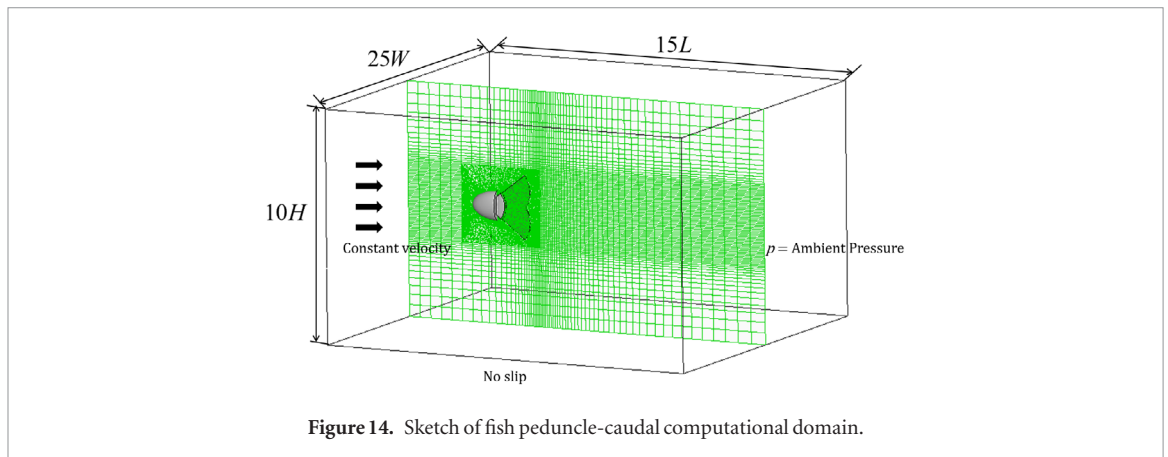
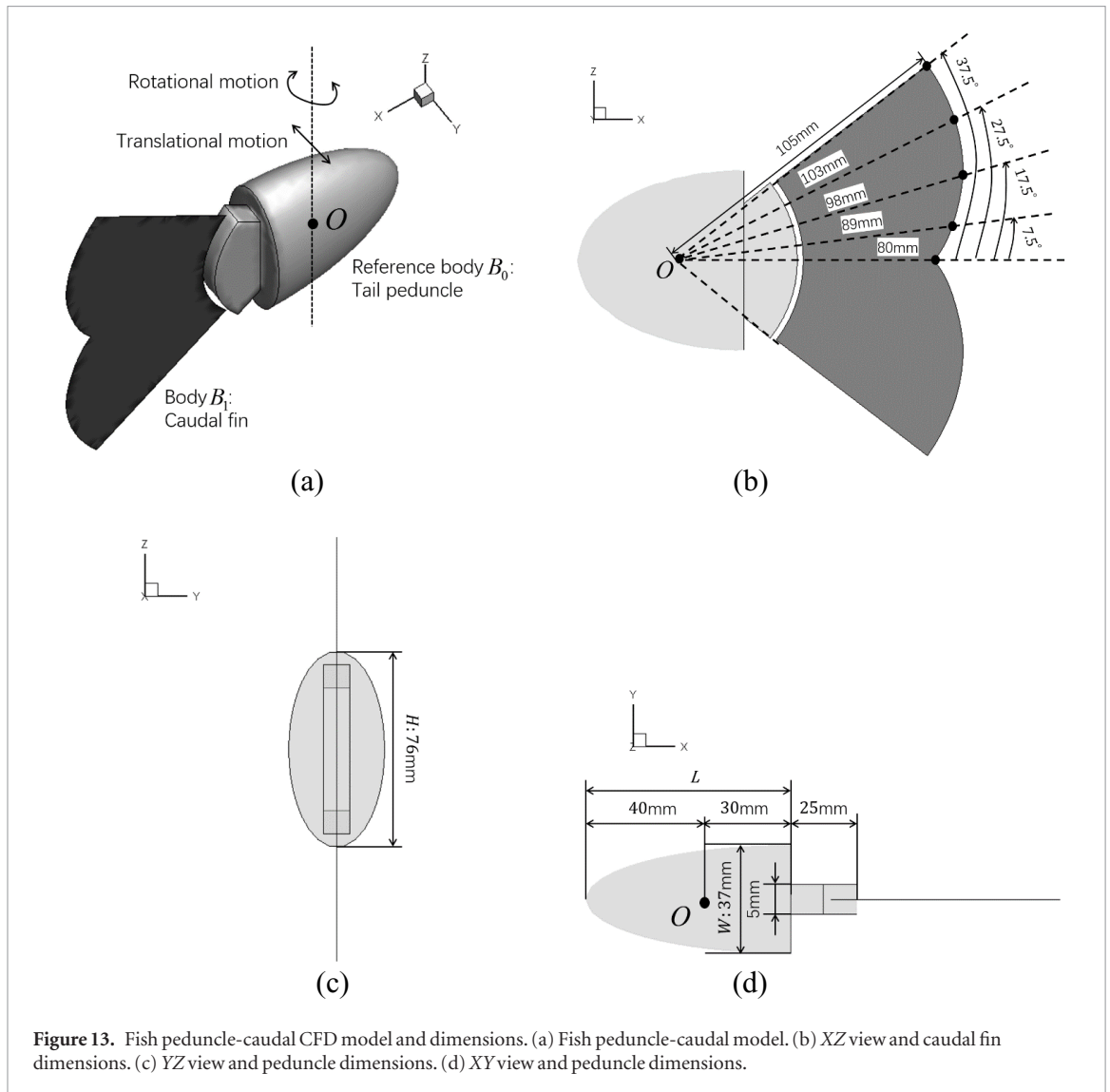
The model is constructed using eight trapezoidal bodies, as shown in figure 7. The length Δs of each body at initial time is identical. Based on the geometry

provided by Carling *et al* [19], the total fish length l is 0.08 m. The width of the whole model is defined as:

$$w_n = 0.0064 - 0.0048(3 - 2s_n/l)s_n^2/l^2 \quad (18)$$

where s_n stands for the distance from the fish head to the current hinge location (n th). The widest length of the model w is at the fish head with a value of 0.0064 m.

At the onset, there is no bending of the fish body, thus its central line is a straight line. Previous studies used a prescribed central line kinematic undulating motion to drive the fish to move forward. The vertical linear motion of the central line was described as:



$$y_n = \frac{s_n/l + 0.25}{1.25} \sin[(s_n/l - t) \cdot 2\pi/T] \quad (19)$$

where y_n stands for the vertical movement of the central line at location s_n [19]. Simulation is carried out at a specific period T of 1.2 s.

To use the present MBD algorithm, the central line motion is converted to a series of angular motions imposed at each virtual hinge. The angular motion

on hinge n is determined by three successive vertical movement y_{n+1} , y_n and y_{n-1} at the location of s_{n+1} , s_n and s_{n-1} , respectively, which is indicated in figure 7 and described by the following equation:

$$\theta_n = \arctan \frac{y_{n+1} - y_n}{\Delta s} - \arctan \frac{y_n - y_{n-1}}{\Delta s}. \quad (20)$$

The variable θ_n is the angular motion on the n th hinge and is given as a known variable into the

MBD algorithm. A transition function β , as shown in equation (21), is utilised in the first undulation period to ensure the angle increases gradually such that no break-down of the iteration could occur due to a dramatic change of angle. Figure 8 displays the prescribed angular motion profiles θ_n at all seven hinges within the first cycle—a transition cycle as discussed above.

$$\theta_n = \beta \hat{\theta}_n$$

$$\beta = \begin{cases} \frac{1 - \cos(\pi t / 1.2)}{2} & 0 \leq t \leq 1.2 \text{ s} \\ 1 & t > 1.2 \text{ s} \end{cases} \quad (21)$$

The simulation is carried out in a domain as presented in figure 9. The model is placed $5l$ away from the outlet boundary. The whole domain is split into inner and outer zones to ensure good mesh quality around the model. No slip boundary is set on the surface of the fish. The pressure at the downstream boundary is given as ambient pressure. The other three boundaries are set as constant velocity ($\vec{u} = (0, 0, 0)$). The mesh in the entire domain is triangular mesh. A time step of $\Delta t = \frac{T}{300}$ is selected for the simulation.

Figure 10 shows the forward and lateral velocity comparisons with Carling *et al* [19]. It is clear that our results compare well with the previous study. As the first undulating period is taken as a transition stage, only the body shape is modified. Thus, the FSI induced forward velocity remains at zero and there is no translational motion of the fish. From the second period onwards, the fish begins to accelerate and then reaches a quasi-stable status.

The vorticity field of the fish swimming within 15 undulating periods is plotted in figure 11 with the existence of a typical reversed Karman Vortex structure. In one undulating period, the beating amplitude of the fish tail has two peaks indicating that the vortex shed twice in one period.

The above comparison between our numerical results and others provides evidence that our developed tool offers a new means to address a continuous fish body undulation via splitting a deformable body into multiple rigid elements.

3.3. Fish peduncle-caudal cupping motion

A series of experimental work has been performed [8, 43] to study the hydrodynamic characteristics of a robotic caudal fin to mimic the homocercal tail of the Bluegill Sunfish. Motions of both peduncle and caudal fin were replicated via a properly designed robotic model as shown in figure 12. The peduncle is connected to a strut, which allows translational and rotational motions. A force and flow visualization experiment was carried out in a small water tunnel using a constant towing speed u . The cupping motion of a passively deformable caudal fin is achieved via fabricating the fin surface using a black silicone membrane and prescribing the motion of each fin ray.

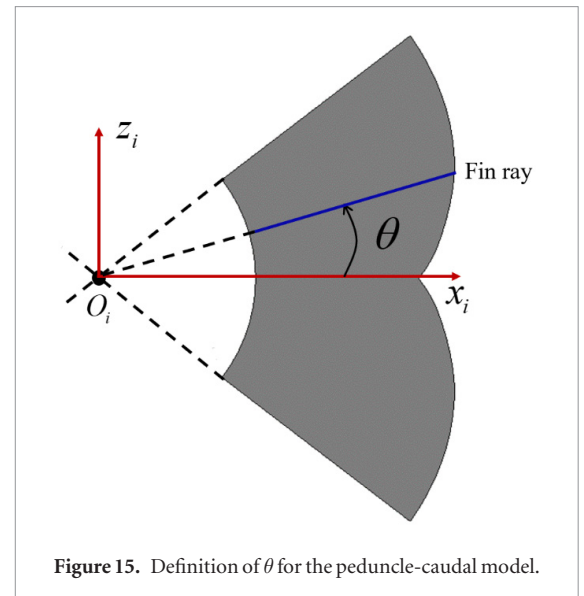


Figure 15. Definition of θ for the peduncle-caudal model.

Table 2. Motion parameters for the peduncle-caudal model.

a_1	a_2	a_3
16	0.4677	0.0068

Based on the experimental model, our CFD model is constructed and displayed in figure 13(a). The caudal fin is modelled as an axisymmetric shape with its thickness omitted. The geometry is defined by providing the chord lengths at four angles (7.5° , 17.5° , 27.5° and 37.5°) in figure 13(b). The caudal peduncle is modelled as a wedged body with three dimensions ($L \times W \times H$) indicated in figures 13(c) and (d).

The computational domain, as shown in figure 14, is large enough to minimise the influence of the outer boundaries. The model is placed $4L$ away from the inlet boundary. Two mesh zones are generated with an inner zone having unstructured tetrahedral elements and an outer zone with structured hexahedral mesh. The total mesh number is approximately 430 000 and the unsteady time step is selected as 500 steps per time period. The inlet boundary is given as a constant velocity, equal to the towing speed during the experiment, which is determined by the Strouhal number, and defined as:

$$St = \frac{f \cdot A}{u} \quad (22)$$

where f , A and u is the frequency, translational motion amplitude and the inlet velocity respectively. The pressure at the right boundary is set to ambient pressure and the surrounding boundary is symmetry. The surface of the peduncle-caudal model is treated as a no slip boundary.

In accordance with the Multi-Body algorithm described in section 2, the present model is considered as a two-element system, i.e. the caudal peduncle (set as the rigid reference body B_0) and the deformable caudal fin (B_1). The caudal fin is connected to the peduncle by a virtual hinge with no rotational motion allowed.

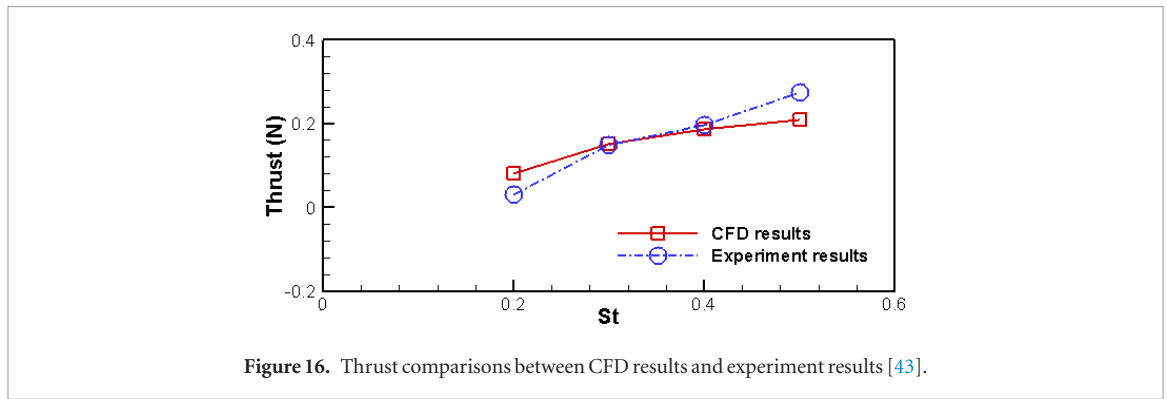


Figure 16. Thrust comparisons between CFD results and experiment results [43].

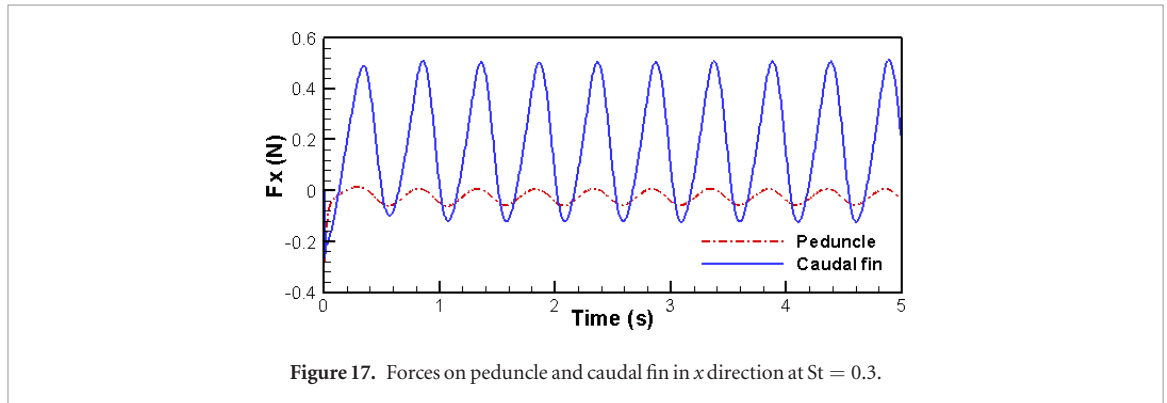


Figure 17. Forces on peduncle and caudal fin in x direction at $St = 0.3$.

Referring to the experiment, the rotational and translational motions are provided on B_0 , as defined in the following equations:

$$\begin{aligned} \text{Translational } S_T &= 0.02 \sin(2\pi t) \\ \text{Rotational } A_R &= 0.2618 \sin(2\pi t - \frac{\pi}{2}). \end{aligned} \quad (23)$$

The cupping motion of the deformable caudal fin can be treated as successive fin rays with different undulating amplitudes, given as:

$$\varphi = A(\theta) \sin(2\pi t) \quad (24)$$

where θ is the angle between each fin ray (blue line in figure 15) and the x axis relative to its local coordinate (red line in figure 15); $A(\theta)$ is the amplitude of each undulating fin ray, described is:

$$A(\theta) = a_1 - a_2\theta + a_3\theta^2. \quad (25)$$

Detailed values of the parameters used in equation (25) are given in table 2 taken from [43].

Simulations are performed for four Strouhal numbers. Figure 16 compares the time averaged thrust between the experiment and CFD modelling at four St , where the thrust is defined as the total force acting on the peduncle and caudal fin in x direction:

$$F_{thrust} = F_{peduncle} + F_{caudal}. \quad (26)$$

As seen from figure 16, the predicted results are consistent with the experiment. Within the St range tested, thrust increases with the St number. A variation of time-dependent force is displayed in figure 17 at $St = 0.3$ for five time periods. Negative values stand for resistance while the positive values reflect propulsion force. Clearly, as indicated by their signs,

peduncle always suffers resistance, possibly due to its blunt shape, while the deformable caudal fin generates propulsion force.

The flow visualization on the instantaneous vortex topology in one motion cycle is shown in figure 18 from two planes. The vortices shed from the caudal fin generate a chain of vortex rings downstream. Further, the vortex rings are linked, which agrees with the findings of Lauder and Drucker [44].

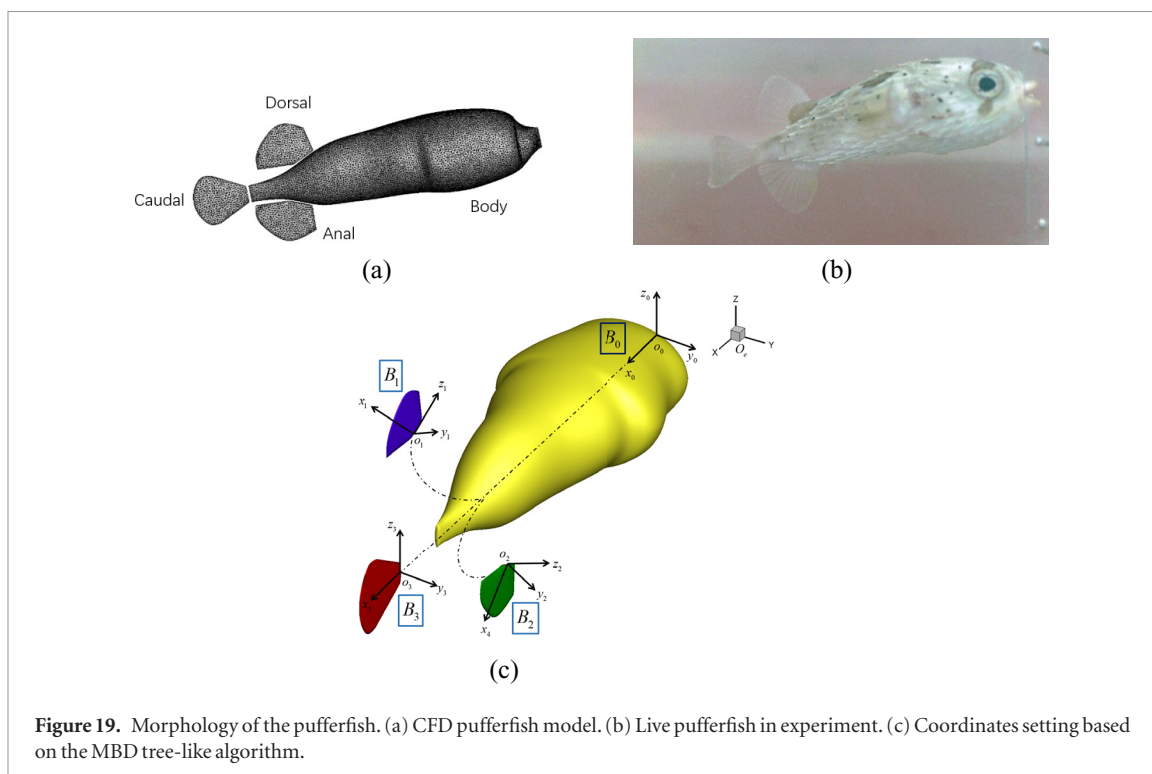
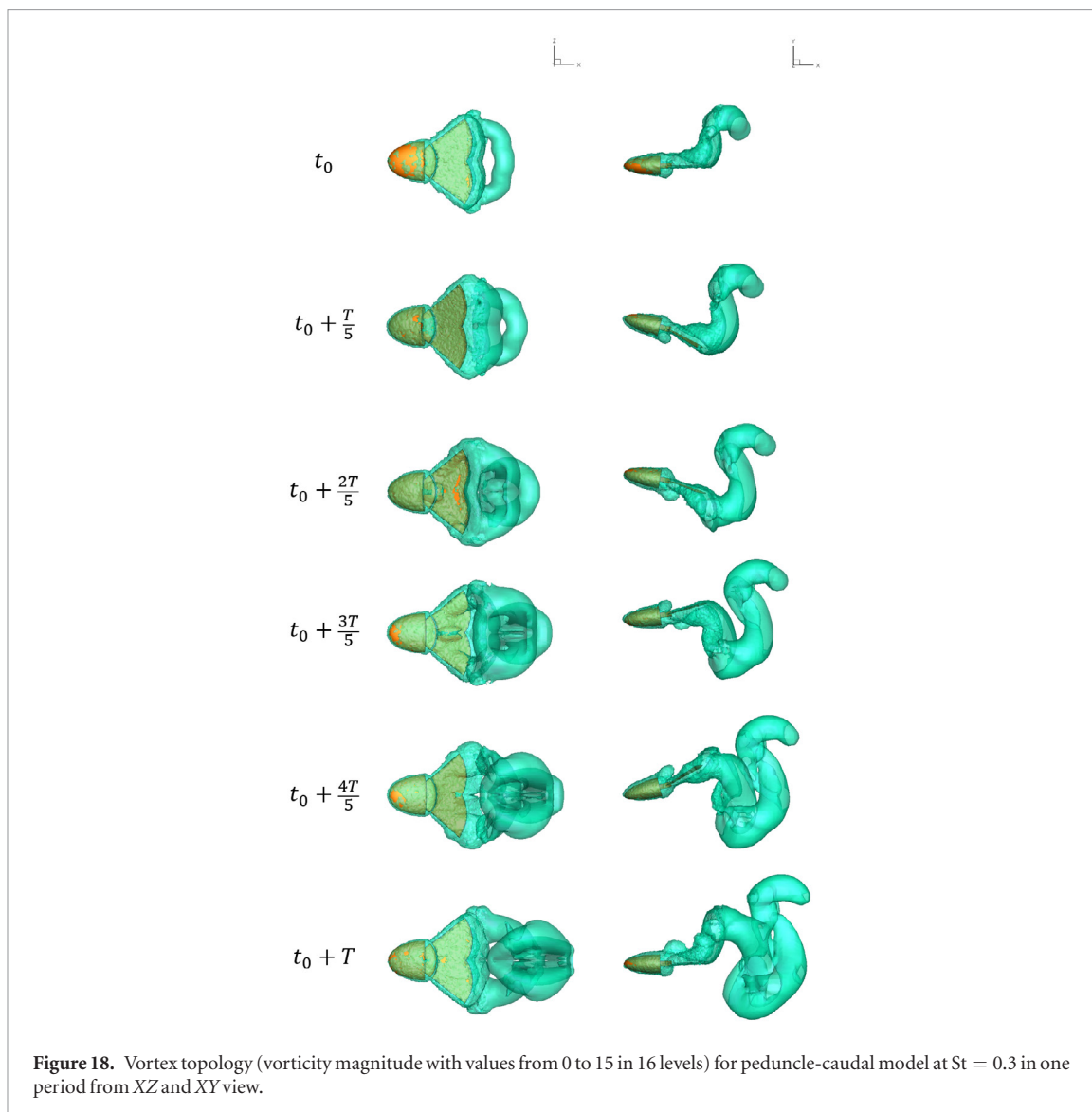
It should be noted that some subtle differences can be observed between the experiment and the CFD at $St = 0.2, 0.5$. This might be caused by the caudal fin edge effect since it has a passive motion in the experiment, while in our CFD modelling the whole surface of the caudal fin is given a prescribed deformation extracted from experimental data.

The quantitative comparison between our CFD prediction and experimental data further demonstrates that the present MBD model can deal with complicated swimming locomotion, including both caudal peduncle rotational translational motions and flexible fin ray undulation.

3.4. Pufferfish with multiple deformable fins

For the sake of ensuring the feasibility of a free moving rigid-deformable MBD system, we apply our code to a self-propulsion fish problem driven by dorsal, anal and caudal fins, such that the fins are considered deformable while the fish body is rigid.

Figure 19(a) shows the numerical model of a 3D pufferfish, which is extracted from the experimental data of a live pufferfish in figure 19(b). Detailed information about the experiment can be referred to in the



paper by Li *et al* [45]. It was observed in the experiment that pectoral fins have subtle movements compared to dorsal and anal fins, and hence the kinematic analysis about the pair of pectoral fins was neglected in Li *et al* [45]. In order to ensure consistency with experimental observations, in the present CFD modelling, the motion of pectoral fins is excluded. However, the method developed herein is able to cope with the dynamic motion of pectoral fins as long as the kinematic data is available from the experiment.

The total length (L) of the model is approximately 0.11 m and the shape of each cross-section of the fish body is close to elliptic. The maximum major and minor-axis of the body are approximately 0.04 m and 0.03 m, respectively. All three fish fins are modelled as wedged surfaces. The density of the fish model is assumed to be the same as that of water, i.e. $\rho_{fish} = \rho_{water}$, which is a reasonable assumption for major aquatic animals. Thus, the influence of gravity and buoyancy may be ignored.

Adopting the established multi-body system concept, this model is considered as a four-element system, as shown in figure 19(c). The fish body is selected as the reference body B_0 and the other three elements are connected to B_0 , numbered as B_2 , B_3 and B_4 for dorsal, anal and caudal fins, respectively.

To model the deformable fish fin, the experimentally measured kinematics are used. The experiments revealed that the dorsal and anal fins undulate in phase with each other, while there is a 180° (π) phase lag between the caudal fin and the other two fins. Each fin is treated as comprising of successive fin rays with a sinusoidal wave travelling from the anterior-most edge down along the fin rays [46]. No deformation along the fin span-wise direction is taken into account. The equation to describe the undulated fin surface is expressed as:

$$\varphi = A(\theta) \sin(\omega t + \psi(\theta)) \quad (27)$$

where θ is the angle between each fin ray (blue line in figure 20) and the x axis relative to its local coordinate (red line in figure 20); $\omega = 32.8 \text{ rad s}^{-1}$ is the undulating frequency; $A(\theta)$ and $\psi(\theta)$ are the undulating amplitude and phase angle of each fin ray, respectively.

For deformable dorsal and anal fins, amplitude and phase angle can be expressed as:

$$\begin{aligned} A(\theta) &= a_1\theta^3 + a_2\theta^2 + a_3\theta + a_4 \\ \psi(\theta) &= p_1\theta^3 + p_2\theta^2 + p_3\theta + p_4. \end{aligned} \quad (28)$$

The prescribed motion of the deformable caudal fin surface can be defined as:

$$\begin{aligned} A_c(\theta) &= a_1 + a_2 \cos(\theta\omega_a) \\ \psi_c(\theta) &= p_1 + p_2 \cos(\theta\omega_p). \end{aligned} \quad (29)$$

Detailed parameters for the kinematics can be found in table 3 and the envelopes of flexible dorsal, anal and caudal fin in one undulating period are shown in figure 21. A time step size $\Delta t = \frac{T}{500}$ is selected for the simulation, where T is the time period and equals 0.192 s.

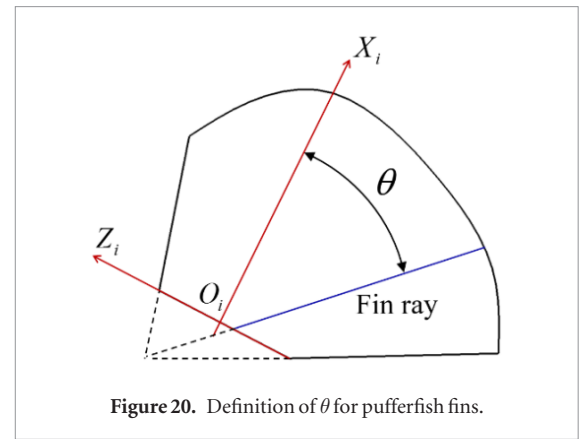


Figure 20. Definition of θ for pufferfish fins.

Table 3. Motion parameters for pufferfish model with multiple fins.

	Amplitude A (rad)		
	Dorsal	Anal	Caudal
ω_a	—	—	6.07
a_1	0.1353	0.0066	0.3861
a_2	0.3204	0.3204	0.3204
a_3	0.3563	0.3563	-
a_4	0.8898	0.8898	-
	Phase angle ψ (rad)		
	Dorsal	Anal	Caudal
ω_p	—	—	—
p_1	0.7247	0.7247	0.7247
p_2	0.2648	0.2648	0.2648
p_3	1.473	1.473	—
p_4	4.106	4.106	—

Figure 22 shows the induced self-propelled fish swimming velocity and displacement in 30 undulating periods. Negative velocity indicates that the fish swims towards ($-x$) direction. The fish accelerates to a quasi-stable stage. The time averaged velocity for the flexible fins are 1.71 BL s^{-1} . Evaluated against the experimental measurement, where 2 BL s^{-1} velocity is obtained for a live fish, our CFD result (1.71 BL s^{-1}) is about 14.5% underestimated. Without considering the possible deformation of the flexible fins in a span-wise direction in our CFD modelling, the predicted final induced swimming velocity is reasonable. This means that our tree-like MBD code can solve the 3D self-propelled fish with median fins.

Apart from the above data which is available from both experiment and CFD methods, our numerical simulation can also provide additional information which is typically difficult to achieve via experimental testing. These include motion displacement, hydrodynamic forces, propulsion efficiency and vortex wake around the fish. As displayed in figure 22, after swimming about 30 cycles, the pufferfish moves about 8 BL towards the negative x direction. The hydrodynamic forces on all three fins and body of the pufferfish is plotted in figure 23, normalized via the following equation:

$$C_f = \frac{F}{\frac{1}{2}\rho_f u_x^2 A} \quad (30)$$

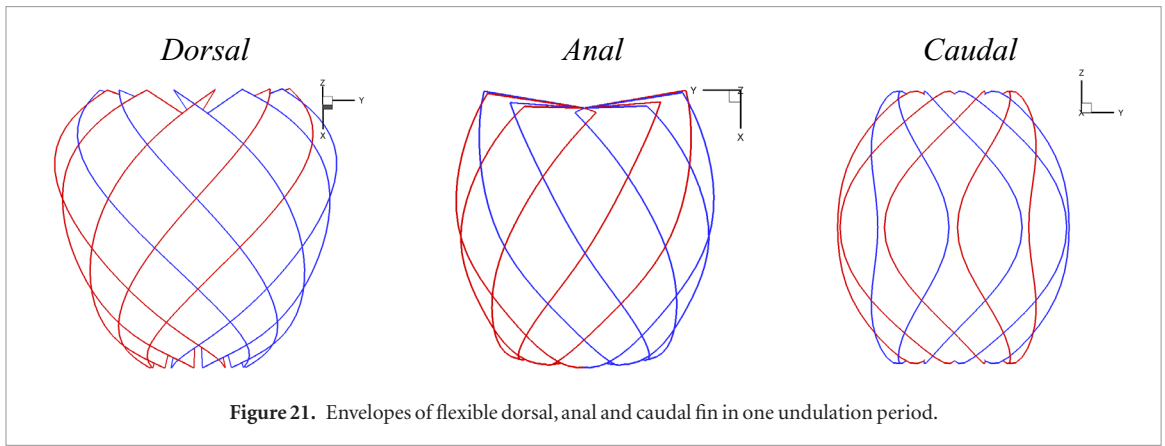


Figure 21. Envelopes of flexible dorsal, anal and caudal fin in one undulation period.

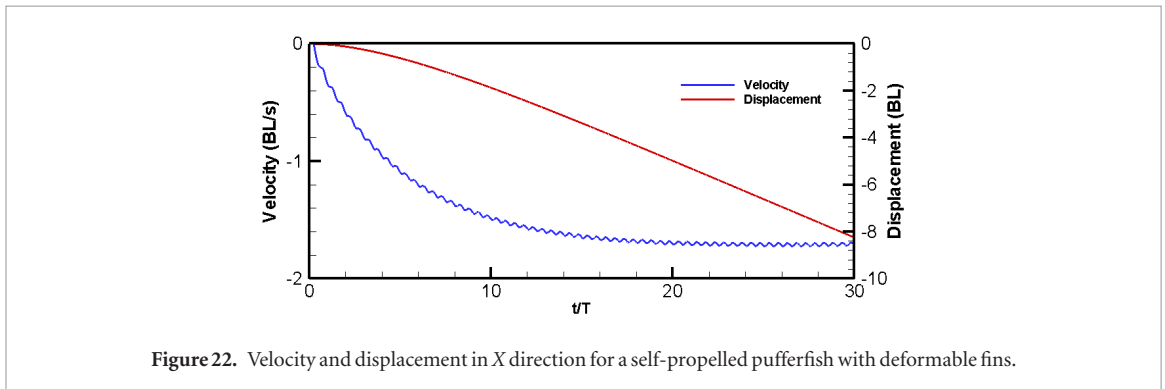


Figure 22. Velocity and displacement in X direction for a self-propelled pufferfish with deformable fins.

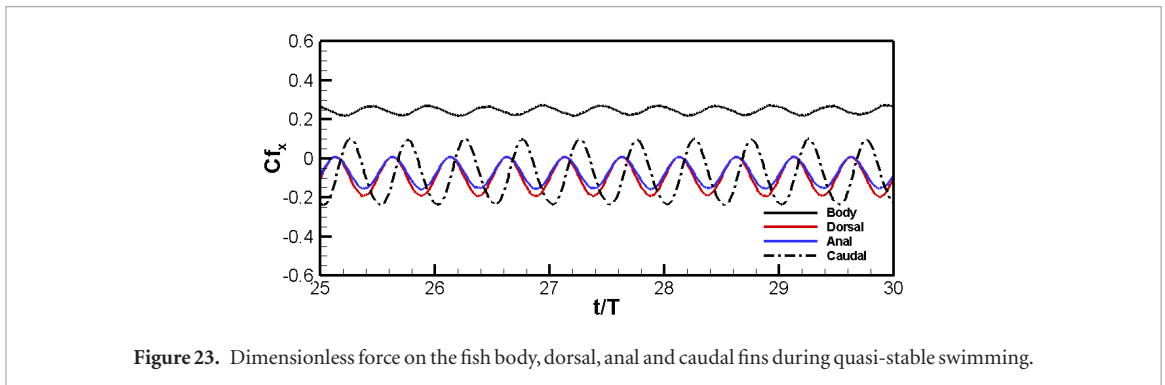


Figure 23. Dimensionless force on the fish body, dorsal, anal and caudal fins during quasi-stable swimming.

where F represents the force, ρ_f is the fluid density, u_x is the time averaged velocity for steady swimming fish and A is the largest crossing area of the fish body. In figure 23, the negative values signify that the generated forces are towards the same direction the fish are swimming. As the fish swims steadily along the negative direction of x , a negative force is a reflection of thrust force, while a positive force is an indication of the drag or resistance force. The thrust generated by the deformable dorsal and anal fins are always negative, while the caudal fin produces a thrust larger than drag. The fish body always suffers drag while swimming.

In terms of propulsion efficiency, it is defined as the mean output power over mean total input power:

$$\eta_{eff} = \frac{\bar{P}_{out}}{\bar{P}_{in}}. \quad (31)$$

As the pufferfish swims towards negative X direction, the output power P_{out} is obtained by multiplying the

total propulsive forces $F_{propulsion-x}$ by the induced time averaged velocity u_x during quasi-stable swimming, shown as:

$$P_{out} = F_{propulsion-x} u_x. \quad (32)$$

The propulsion force $F_{propulsion-x}$ is considered as being generated by dorsal $F_{dorsal-x}$, anal F_{anal-x} and caudal fins $F_{caudal-x}$:

$$F_{propulsion-x} = F_{dorsal-x} + F_{anal-x} + F_{caudal-x}. \quad (33)$$

The total input power P_{in} is defined by the multiplication of the torque τ and the angular velocity $\dot{\varphi}$:

$$P_{in} = \sum (\vec{\tau} \cdot \vec{\dot{\varphi}}). \quad (34)$$

Torque τ is obtained by integrating the moment of pressure force along the fin's rotation axis over each fin surface. For the deformable fin, the averaged angular velocity $\dot{\varphi}$ of the whole fin surface is used. The time

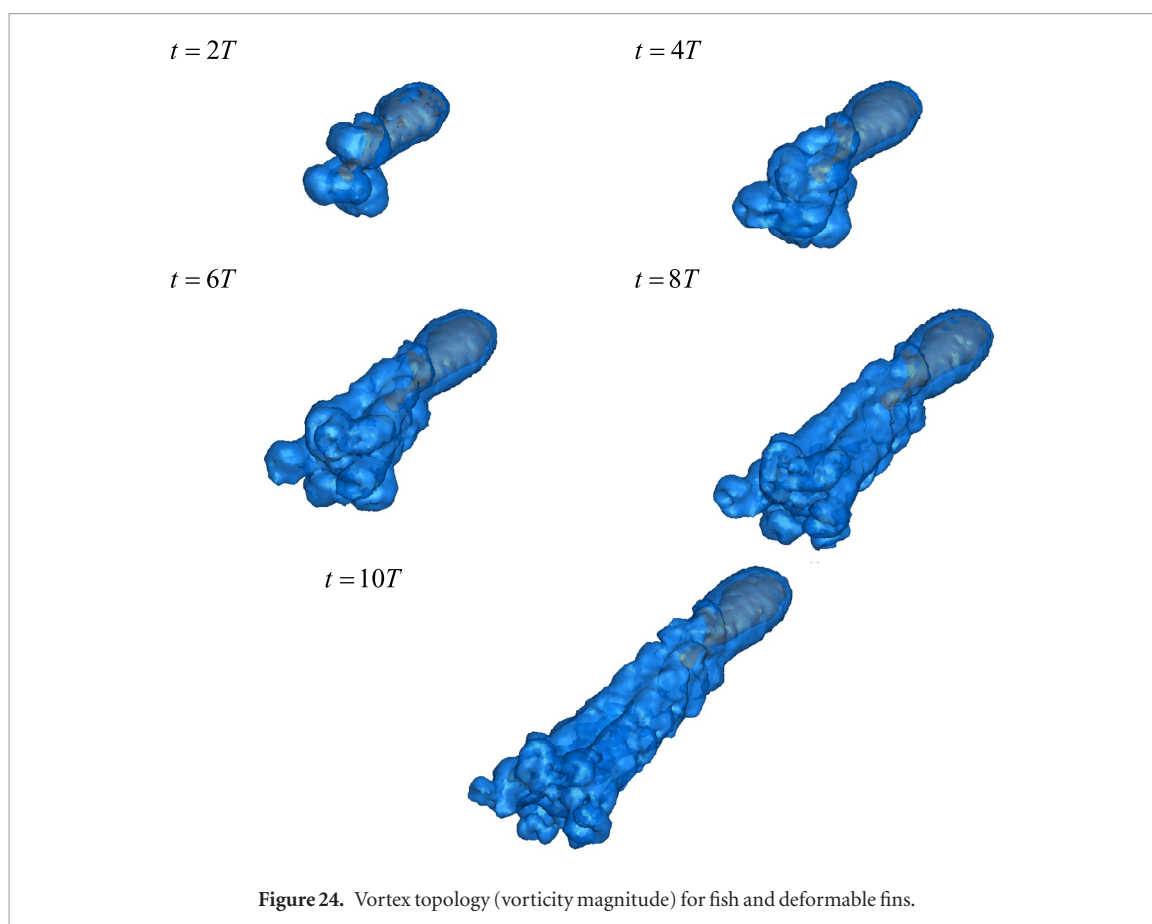


Figure 24. Vortex topology (vorticity magnitude) for fish and deformable fins.

averaged input and output power is 1.79 mW and 0.8 mW, respectively. Thus, the efficiency is 45.44%.

Detailed vorticity contour for deformable fins is displayed in figure 24. It is observed that dorsal and anal fins generate vortex, as does the caudal fin. Flow visualization results reveal that apparent interactions among caudal, dorsal and anal fins can be found for deformable fins.


4. Conclusion

In this work, we presented a newly developed method to solve bio-inspired swimming problems. The locomotion of fish and fins is simulated using a multi-body dynamic theory and the fluid flow field around the fish is investigated with a CFD numerical method. Four case studies were tested, including a three-linked rigid-body swimmer, one anguilliform fish model, a cupping motion of a caudal fin and a self-propelled pufferfish with dorsal, anal and caudal fins. Our research relates to previous studies on the undulating motion of both a discrete eel-like model and a continuous eel-like body, single caudal fin oscillation and fish swimming induced by multiple fins' undulation. Numerical results are compared with data from other available resources and good comparisons are made. We have shown that this new modelling tool can be applied to comprehensive studies on fish swimming behaviour via either the undulating or oscillating motion of both fish body and different types of rigid/deformable fins.

Acknowledgements

Results were obtained using the EPSRC funded ARCHIE-WeSt High Performance Computer (www.archie-west.ac.uk). EPSRC grant no. EP/K000586/1. Hao Liu is partly supported by the Grant-in-Aid for Scientific Research on Innovative Areas of No. 24120007, JSPS. Kainan Hu and Li Wen are supported by the National Science Foundation, China (grant no. 61633004 and 61333016). Authors would like to acknowledge Professor Frédéric Boyer and Dr Mathieu Porez at Institut de Recherche en Communication et Cybernétique de Nantes (IRCCyN) for their initial support to our multi-body dynamics development. The authors are also grateful to the UK Royal Academy Engineering for partial support of this work.

ORCID iDs

Ruoxin Li  <https://orcid.org/0000-0003-3313-6652>
 Hao Liu  <https://orcid.org/0000-0002-8687-3237>
 Li Wen  <https://orcid.org/0000-0002-1498-3103>

References

- [1] Scaradozzi D, Palmieri G, Costa D and Pinelli A 2017 BCF swimming locomotion for autonomous underwater robots: a review and a novel solution to improve control and efficiency *Ocean Eng.* **130** 437–53
- [2] Roper D T, Sharma S, Sutton R and Culverhouse P 2011 A review of developments towards biologically inspired

- propulsion systems for autonomous underwater vehicles *Proc. Inst. Mech. Eng. M* **225** 77–96
- [3] Webb P W 1994 The biology of fish swimming *The Mechanics and Physiology of Animal Swimming* ed L Maddock et al (Cambridge: Cambridge University Press) pp 45–62
- [4] Webb P W 1984 Form and function in fish swimming *Sci. Am.* **251** 72–82
- [5] Sfakiotakis M, Lane D M and Davies J B C 1999 Review of fish swimming modes for aquatic locomotion *IEEE J. Ocean. Eng.* **24** 237–52
- [6] Lauder G V 2015 Fish locomotion: recent advances and new directions *Annu. Rev. Mar. Sci.* **7** 521–45
- [7] Liu H, Kolomenskiy D, Nakata T and Li G 2017 Unsteady bio-fluid dynamics in flying and swimming *Acta Mech. Sin.* **33** 663–84
- [8] Ren Z, Hu K, Wang T and Wen L 2016 Investigation of fish caudal fin locomotion using a bio-inspired robotic model *Int. J. Adv. Robot. Syst.* **13** 87–96
- [9] Porez M, Boyer F and Ijspeert A J 2014 Improved lighthill fish swimming model for bio-inspired robots: modeling, computational aspects and experimental comparisons *Int. J. Robot. Res.* **33** 1322–41
- [10] Drucker E G and Lauder G V 2001 Locomotor function of the dorsal fin in teleost fishes: experimental analysis of wake forces in sunfish *J. Exp. Biol.* **204** 2943–58
- [11] Drucker E G and Lauder G V 2005 Locomotor function of the dorsal fin in rainbow trout: kinematic patterns and hydrodynamic forces *J. Exp. Biol.* **208** 4479–94
- [12] Standen E M and Lauder G V 2005 Dorsal and anal fin function in bluegill sunfish *Lepomis macrochirus*: three-dimensional kinematics during propulsion and maneuvering *J. Exp. Biol.* **208** 2753–63
- [13] Drucker E G and Lauder G V 2000 A hydrodynamic analysis of fish swimming speed: wake structure and locomotor force in slow and fast labriform swimmers *J. Exp. Biol.* **203** 2379–93
- [14] Flammang B E, Lauder G V, Troolin D R and Strand T 2011 Volumetric imaging of shark tail hydrodynamics reveals a three-dimensional dual-ring vortex wake structure *Proc. R. Soc. B* **278** 3670–8
- [15] Müller U K, van den Boogaart J G M and van Leeuwen J L 2008 Flow patterns of larval fish: undulatory swimming in the intermediate flow regime *J. Exp. Biol.* **211** 196–205
- [16] Lighthill M J 1971 Large-amplitude elongated-body theory of fish locomotion *Proc. R. Soc. B* **179** 125–38
- [17] Li G, Müller U K, van Leeuwen J L and Liu H 2016 Fish larvae exploit edge vortices along their dorsal and ventral fin folds to propel themselves *J. R. Soc. Interface* **13** 20160068
- [18] Kern S and Koumoutsakos P 2006 Simulations of optimized anguilliform swimming *J. Exp. Biol.* **209** 4841–57
- [19] Carling J, Williams T L and Bowtell G 1998 Self-propelled anguilliform swimming: simultaneous solution of the two-dimensional Navier–Stokes equations and Newton’s laws of motion *J. Exp. Biol.* **201** 3143–66
- [20] Li G, Müller U K, van Leeuwen J L and Liu H 2012 Body dynamics and hydrodynamics of swimming fish larvae: a computational study *J. Exp. Biol.* **215** 4015–33
- [21] Borazjani I, Sotiropoulos F, Tytell E D and Lauder G V 2012 Hydrodynamics of the bluegill sunfish C-start escape response: three-dimensional simulations and comparison with experimental data *J. Exp. Biol.* **215** 671–84
- [22] Li G, Müller U K, van Leeuwen J L and Liu H 2014 Escape trajectories are deflected when fish larvae intercept their own C-start wake *J. R. Soc. Interface* **11** 20140848
- [23] Eldredge J D 2008 Dynamically coupled fluid–body interactions in vorticity-based numerical simulations *J. Comput. Phys.* **227** 9170–94
- [24] Maertens A P, Gao A and Triantafyllou M S 2017 Optimal undulatory swimming for a single fish-like body and for a pair of interacting swimmers *J. Fluid Mech.* **813** 301–45
- [25] Ogata Y, Azama T and Moriyama Y 2017 Numerical investigation of small fish accelerating impulsively to terminal speed *J. Fluid Sci. Technol.* **12** JFST0009
- [26] Curatolo M and Teresi L 2016 Modeling and simulation of fish swimming with active muscles *J. Theor. Biol.* **409** 18–26
- [27] Li N and Su Y 2016 Fluid dynamics of biomimetic pectoral fin propulsion using immersed boundary method *Appl. Bionics Biomech.* **2016** 22
- [28] Zhang Y, He J and Low K-H 2013 Numeric simulation on the performance of an undulating fin in the wake of a periodic oscillating plate *Int. J. Adv. Robot. Syst.* **10** 328–40
- [29] Zhu Q and Shoele K 2008 Propulsion performance of a skeleton-strengthened fin *J. Exp. Biol.* **211** 2087–100
- [30] Shoele K and Zhu Q 2009 Fluid–structure interactions of skeleton-reinforced fins: performance analysis of a paired fin in lift-based propulsion *J. Exp. Biol.* **212** 2679–90
- [31] Shoele K and Zhu Q 2010 Numerical simulation of a pectoral fin during labriform swimming *J. Exp. Biol.* **213** 2038–47
- [32] Akhtar I, Mittal R, Lauder G V and Drucker E 2007 Hydrodynamics of a biologically inspired tandem flapping foil configuration *Theor. Comput. Fluid Dyn.* **21** 155–70
- [33] Shoele K and Zhu Q 2015 Performance of synchronized fins in biomimetic propulsion *Bioinspir. Biomim.* **10** 026008
- [34] Borazjani I 2013 The functional role of caudal and anal/dorsal fins during the C-start of a bluegill sunfish *J. Exp. Biol.* **216** 1658–69
- [35] Han P, Liu G, Ren Y and Dong H 2016 Computational analysis of 3D fin–fin interaction in fish’s steady swimming *ASME 2016 Fluids Engineering Division Summer Meeting FEDSM2016-7699* (Washington, DC, USA) p V01AT04A006
- [36] Xu Y and Wan D 2012 Numerical simulation of fish swimming with rigid pectoral fins *J. Hydrodynam.* **B** **24** 263–72
- [37] Khalil W and Dombre E 2004 *Modeling, Identification and Control of Robots* (Oxford: Butterworth-Heinemann)
- [38] Hu J, Xiao Q and Nguyen V T 2013 An exploration of a PASSIVE articulated fish-like system *ASME 2013 32nd Int. Conf. on Ocean, Offshore and Arctic Engineering OMAE2013-10808* (Nantes, France) p V005T06A059
- [39] Hu J 2016 Numerical study on hydrodynamic performance of bio-mimetic locomotion *PhD Thesis* University of Strathclyde, Glasgow, Scotland, UK
- [40] Porez M, Boyer F and Belkhir A 2014 A hybrid dynamic model for bio-inspired robots with soft appendages-application to a bio-inspired flexible flapping-wing micro air vehicle *IEEE Int. Conf. on Robotics and Automation (ICRA ’2014)* (Hong Kong) pp 3556–63
- [41] Boyer F and Porez M 2015 Multibody system dynamics for bio-inspired locomotion: from geometric structures to computational aspects *Bioinspir. Biomim.* **10** 025007
- [42] Khalil W, Boyer F and Morsli F 2017 General dynamic algorithm for floating base tree structure robots with flexible joints and links *J. Mech. Robot.* **9** 031003
- [43] Hu K, Ren Z, Wang Y, Wang T and Wen L 2016 Quantitative hydrodynamic investigation of fish caudal fin cupping motion using a bio-robotic model *2016 IEEE Int. Conf. on Robotics and Biomimetics (ROBIO)* pp 295–300
- [44] Lauder G V and Drucker E G 2002 Forces, fishes, and fluids: hydrodynamic mechanisms of aquatic locomotion *Physiology* **17** 235–40
- [45] Li L, Li G, Li R, Xiao Q and Liu H 2018 Multi-fin kinematics and hydrodynamics in pufferfish steady swimming *Ocean Eng.* **158** 111–22
- [46] Gordon M, Plaut I and Kim D 1996 How puffers (Teleostei: Tetraodontidae) swim *J. Fish Biol.* **49** 319–28
- [47] Kanso E, Marsden J E, Rowley C W and Melli-Huber J B 2005 Locomotion of articulated bodies in a perfect fluid *J. Nonlinear Sci.* **15** 255–89